ADVANCED MATERIALS INTERFACES
Open Access
www.advmatinterfaces.de



# Machine Learning-Accelerated Reconstruction of Periodic Nanostructures with X-ray Fluorescence Spectroscopy Methods

*Vinh-Binh Truong,* Analía Fernández Herrero, Kas Andrle, Victor Soltwisch, and Philipp Hönicke*

**With advancements in the semiconductor industry, the complexity of three-dimensional (3D) nanostructures becomes higher with continuously decreasing feature sizes. In order to monitor the processing steps, it is crucial to accurately determine the critical dimensions and composition of these nanostructures. Early detection of production malfunctions is crucial for reasonable production yields, as even minor imperfections can heavily impede device performance. Grazing X-ray fluorescence spectroscopy methods are non-destructive and element-specific methods with high sensitivity for nanostructured surfaces. They enable the quantification and localization of elements within the sample, with information depths sufficient also for buried features. Such measurements can be utilized to reconstruct the shape and size of nanostructure features, with simulated data based on finite element method (FEM) Maxwell calculations. However, the computation time of FEM calculations poses a challenge (especially in the X-ray energy regime), prolonging the reconstruction process and making it impractical for the characterization of multiple samples. To address this issue, a neural network-based approach is adopted to replace the time-consuming FEM-based forward calculations. In this study, the feasibility of utilizing neural networks for nanostructure reconstruction is demonstrated on various nanostructures. The discrimination limit for different model parameters is assessed and compared against conventional FEM calculation results.**

## 1. Introduction

Recent developments in nanotechnology have significantly influenced the semiconductor industry, driving a relentless pursuit for smaller and more complex nanostructures.[1–3] This quest for miniaturization and enhanced performance has increased the need for metrology techniques capable of characterizing these structures with sub-nm precision.[4] This precision is needed while minor imperfections or defects from manufacturing can translate to massive performances losses or even failures in the final devices.[5] Among these challenges, the characterization of buried nanostructures stands out as an emerging field, due to the rise of new technologies such as gate-all-around (GAA), forksheet and complementary field-effect transistors (CFET).[6–8]

Conventional metrology tools like atomic force microscopy (AFM), transmission electron microscopy (TEM) and scanning electron microscopy (SEM) are widely used for the characterization of semiconductor materials and devices.[9–11] However, as feature sizes shrink and structures become increasingly complex, these traditional methods face limitations in terms of either resolution, buried feature sensitivity or their destructive nature.[4,12] It was recently shown, that critical dimension small-angle X-ray scattering (CDSAXS) and grazing incidence small-angle X-ray scattering (GISAXS) provide valuable insights into the morphology and dimensions of nanostructures while also probing larger sample areas in a non-destructive manner.[13–15] However, these methods rely on a high optical contrast to discriminate between different elements, which can emerge as valuable aspect for the characterization of buried nanostructures.

In this context, grazing incidence X-ray fluorescence spectroscopy (GIXRF) and particularly grazing exit X-ray fluorescence spectroscopy (GEXRF) emerge as promising alternative metrology techniques.[16,17] By exploiting the characteristic fluorescence emission, both methods offer element-specific, non-destructive and surface-sensitive characterizations.[18–20] During the GIXRF

V.-B. Truong, A. F. Herrero, V. Soltwisch, P. Hönicke
Physikalisch-Technische Bundesanstalt - National Metrology Institute
Abbestr. 2-12, 10587 Berlin, Germany
E-mail: vinh-binh.truong@ptb.de
K. Andrle
Lawrence Berkeley National Laboratory
1 Cyclotron Road, Berkeley, CA 94720, USA
P. Hönicke
Helmholtz Zentrum Berlin für Materialien und Energie
Hahn-Meitner-Platz 1, 14109 Berlin, Germany

The ORCID identification number(s) for the author(s) of this article can be found under https://doi.org/10.1002/admi.202400898



**DOI: 10.1002/admi.202400898**

measurement the sample is illuminated at grazing or shallow angles. Due to interference effects between the incident and reflected beam, an X-ray standing wave (XSW) field is formed with pronounced intensity modulations in the emerging nodes and anti-nodes.[21,22] By changing the incident angle of the beam to the sample surface, the penetration depth of the XSW field can be varied, probing the near-surface area of the sample.

One limitation of this technique is caused by the large beam footprint projected onto the sample, which results into an over-illumination of small regions of interest, often found on semiconductor samples (order of 100 µm × 100 µm or smaller). GEXRF circumvents this limitation with the near-normal incident angle of the excitation beam, making this technique favorable for these samples.[17] The emitted fluorescence signal is measured in dependence of the emission angles and can also be used for the subsequent reconstruction of the nanotructure. Recent studies have demonstrated successful reconstructions of nanostructures utilizing both techniques, showcasing their potential as a powerful tool for semiconductor metrology.[17,23–26]

Despite their shown potential, the wider adaptation of these methods in respect to nanostructure characterization faces significant challenges. One of the challenges is to simulate the effects of the emerging XSW field within a modeling step that utilizes a finite-element method (FEM) Maxwell calculation.[27] This mesh-based evaluation is needed to accurately calculate the electric field distribution of the XSW, in presence of features such as roundings and sidewall angles, which typically occur in the description of nanostructures. The FEM calculation is computationally expensive, impeding the whole evaluation process in terms of computation speed. This intensely limits the viability of these techniques for nanostructure characterization in an industrial environment.

However, with the recent rise of neural networks (NNs), a new opportunity for fast computation of complex problems and modeling emerges. Their ability to learn complex relationships and mapping from data allow them to solve challenging problems with far less computation time.[28–30] This upside can be exploited in physics-based problems, where an accurate simulation of the problem would demand too many computational resources. Particularly in the field of optics they have proven to be highly beneficial. For example, it was shown that the incorporation of neural networks within a deep reinforcement learning framework can optimize the design process of dielectric multilayer stacks for specific optical applications.[31,32] Furthermore, neural networks have been utilized to model the interaction between incident light and matter, offering a computationally efficient alternative to conventional, resource-intensive simulation methods.[33–35]

In this work, a neural network model was utilized to circumvent the time-consuming FEM calculation required for the nanostructure reconstruction. The network was trained to directly predict the fluorescence intensities from an arbitrary set of geometrical parameters from the nanostructure. By substituting the time-consuming FEM calculations with the neural network model, the required computation time was reduced by several orders of magnitude (approximately $10^{-4}$). To validate the feasibility of this approach, a study was conducted on three different $Si_3N_4/SiO_2$ nanogratings with varying geometrical parameters. The samples were measured using GIXRF and reconstructions obtained with the NN and FEM forward calculations were compared with each other. The results show that the NN model is a suitable substitution for the time-consuming FEM calculations, yielding reconstruction results close to the latter approach.

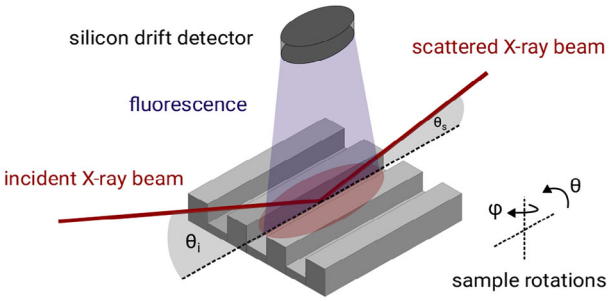


**Figure 1.** Concept of the experimental setup for the GIXRF measurements. The SDD detector (normal to the sample surface) captures the emitted fluorescence photons which were excited by the XSW-field. The investigated sample can be rotated in $\theta$- and $\varphi$-direction in respect to the incident excitation beam.

According to the Helmholtz reciprocity principle, a GEXRF measurement can be analyzed from the perspective of GIXRF.[20,36] In this context, the point of fluorescence emission is treated as a source and the emitted electric field is evaluated at the detector plane. Consequently, a GEXRF experiment can be simulated analogously to a GIXRF simulation, with the primary distinction being the substitution of the incident source energy with the emitted fluorescence line energy. This principle allows the neural network approach to be easily extended to GEXRF measurements, which also depend on a FEM modeling step during the reconstruction process. The following results underline the feasibility of neural networks for a fast evaluation process in future metrology applications, particularly when traditional modeling techniques are computationally prohibitive.

## 2. Measurement Technique

In this work, three $Si_3N_4/SiO_2$ line nanogratings with slightly varying critical dimensions (*cd*) were investigated with GIXRF. This technique relies on the formation of an XSW field that is originating from the interference of the incident and reflected beam.[37] A big advantage of this method is the high sensitivity on the incident and azimuthal angles (in $\theta$- and $\varphi$-direction) which allows for a precise near-surface sampling due to the tuneable penetration depth of the XSW.[16] The XSW field functions as a nanoscale sensor which can probe the dimensions of the investigated nanostructure.

An illustration of the experimental setup is shown in **Figure 1**. The measurements were done at the plane-grating monochromator (PGM) beamline (at BESSY II electron storage ring in the PTB laboratory) which provided undulator radiation for the measurements.[38,39] The energy of the incident beam was $E = 680$ eV which is sufficient to excite both the oxygen and nitrogen inside the nanograting material. At first, the sample was aligned to an incident angle of $\theta = 0°$ and azimuthal angle of $\varphi = 0°$, ensuring an orientation of the nanograting lines parallel to the beam direction. Different incident angles $\theta$ and angular $\varphi$-rotations can be performed by the nine-axis manipulator inside the ultrahigh-vacuum chamber.[40] A calibrated silicon drift de-

 

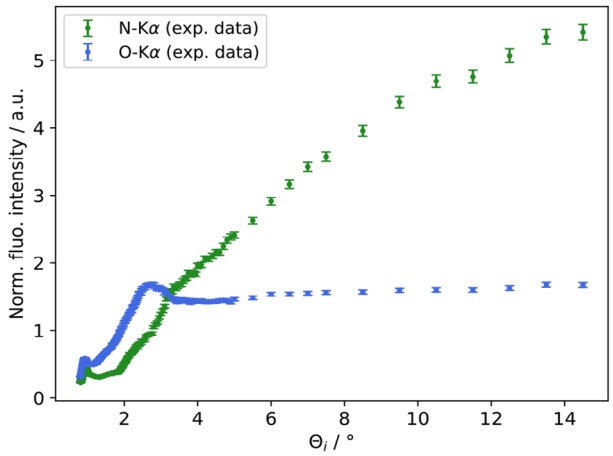


**Figure 2.** Experimental data obtained from the GIXRF measurements. Showcased are the measured N–$K_\alpha$ and O–$K_\alpha$ fluorescence signals of the $Si_3N_4/SiO_2$ nanograting. The fluorescence signal was normalized by the mean value of the respective curve. The experimental error is attributed to the counting statistic error $\sigma_I$ and error of solid angle $\sigma_\Omega$.

tector (SDD) is mounted perpendicular to the sample surface, to record a fluorescence spectrum at each angular combination of $\theta$ and $\varphi$. The incident X-ray beam forms an XSW field with the reflected beam, which excites fluorescence photons within the nanograting material. Only fluorescence photons that are emitted within the solid angle of the SDD can be detected. The incident photon flux $\Phi_0$ was monitored by a calibrated photodiode during the measurement.

**Figure 2** shows an example of the experimental data obtained from the GIXRF measurements of the $Si_3N_4/SiO_2$ nanogratings. Displayed are the measured N-$K_\alpha$ and O-$K_\alpha$ fluorescence signals which were further normalized by their mean intensity value over the angular range, accordingly to

$$I_{\text{norm}}(\theta_k) = \frac{I(\theta_k)}{\frac{1}{n}\sum_i^n I(\theta_i)} \tag{1}$$

The angular range was sampled with step sizes between 0.01° to 0.1° for small angles between 0.82° to 5° to ensure that surface-sensitive features are well captured and resolved within the fluorescence signals. With increasing incident angles, the fluorescence signal follows a saturation behavior which allows to reduce the measurement points for higher incident angles with bigger step sizes of 0.5°. An azimuthal angle of $\varphi = 0°$ was chosen to align the grating lines parallel to the plane of incidence.

The error from the counting statistic $\sigma_I = \sqrt{I}/I$ and the solid angle error $\sigma_\Omega$ contribute to the total experimental error $\sigma_{\text{exp}}$ accordingly to

$$\sigma_{\text{exp}} = \sqrt{{\sigma_I}^2 + {\sigma_\Omega}^2} \tag{2}$$

The initial peak, positioned around $\theta_i = 1°$, can be observed in both datasets. At this specific angle, the first mode of the XSW field fully occupies the space between the gratings.[41] Near-surface atoms become excited, emitting fluorescence photons and leading to an initial increase of the signal. As the angle of incidence increases, additional modes of the XSW field enter the nanostructure, enhancing material excitation and resulting in an increased fluorescence signal. However, in the case of the oxygen signal, a second peak is visible at $\theta_i = 2.85°$. Here, one mode penetrates the $SiO_2$ material on the top of the nanostructure, while modes inside the groove fill the oxide material at the bottom of the nanostructure, leading to an increase of the measured oxygen signal.[41]

Due to the thin $SiO_2$ layer (few nm) on top of the nanostructure, a saturation is observable in the oxygen signal. Contrary to that is the nitrogen signal, that steadily increases with higher incident angles. This can be explained by the sheer size of the $Si_3N_4$ nanostructure, where more material can become excited with increasing penetration depth of the XSW field. However, for fluorescence photons emitted from deep inside the material, self-absorption effects become relevant. This is observable in the nitrogen signal, where a slight saturation is noticeable for very large incident angles.

## 3. Inverse Problem and Modeling

### 3.1. Reconstruction Process

The reconstruction of the nanostructures requires to approach an inverse problem, in which the initial state of the system is unknown and must be derived from the observed data. For this kind of task it is necessary to solve the problem in a reverse manner and deduct the true solution from assumptions of the initial sample system. **Figure 3** displays the workflow of the applied reconstruction process which can be divided into the following steps.

- **Model assumption**: The algorithm starts with an assumption of the nanostructure model. The model is defined by a parameter vector $\vec{p} = \{h, cd, swa, t_{\text{oxide}}, t_{\text{groove}}\}$ which changes the geometry of the nanostructure. **Figure 4a** depicts the nanostruc-

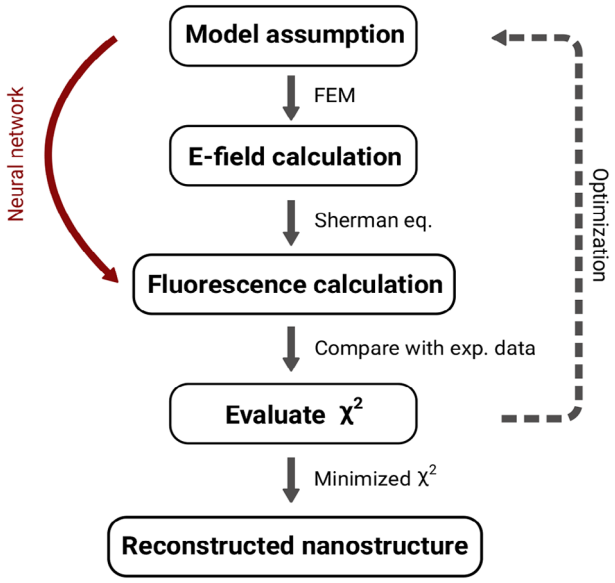


**Figure 3.** Flowchart of reconstruction process. A neural network is utilized to circumvent the computationally expensive FEM calculation that is needed for the electric near-field calculation.

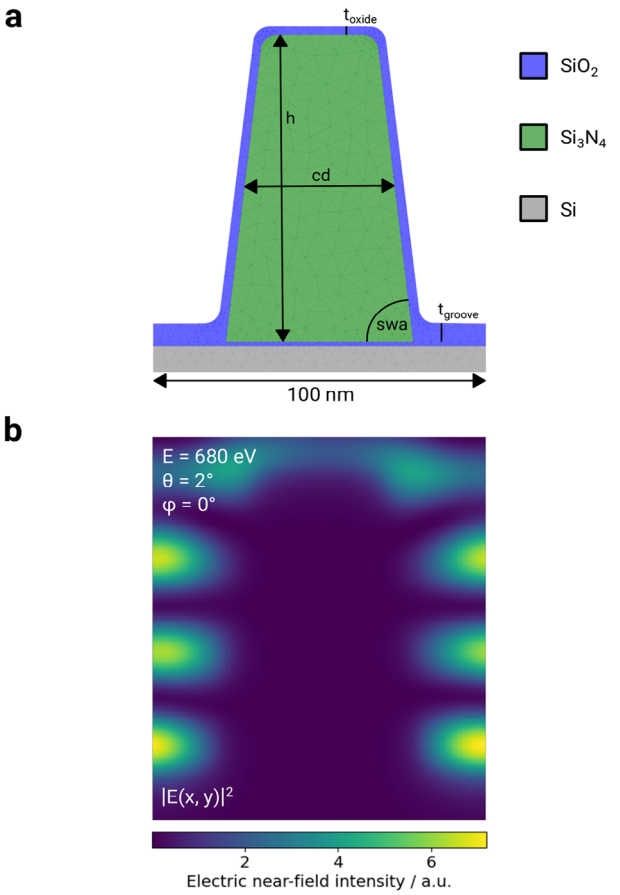


**Figure 4.** a) Model of the $Si_3N_4/SiO_2$ nanograting sample. The model is parameterized by the *h* (height), *cd* (width), *swa* (sidewall angle), thickness of the $SiO_2$ layer on top $t_{oxide}$ and in the groove $t_{groove}$ of the nanostructure. The pitch between grating lines consists of 100 nm. b) 2D cross-sectional calculation of the electric near-field intensity distribution of the nanostructure. Periodic boundary conditions were assumed on the sides of the nanostructure.

ture model which was used for the simulations. The five model parameters (*h* height, *cd* width/critical dimension, *swa* sidewall angle and $t_{oxide}/t_{groove}$ oxide thicknesses) were chosen to be best describing the $Si_3N_4/SiO_2$ nanograting, due to their high sensitivity within the O-$K_\alpha$ and N-$K_\alpha$ fluorescence signals which are emitted from the nanostructure. The parameters *h*, *cd* and *swa* define the shape of the $Si_3N_4$ bulk structure and therefore the total excited area for the N-$K_\alpha$ fluorescence emission. Whereas the O-$K_\alpha$ fluorescence signal can be parameterized by two different $SiO_2$ thicknesses on either the nanostructure and within the grating grooves. The $SiO_2$ layer thickness on top of the Si base substrate was kept constant (1.35 nm) as this parameter showed low sensitivity on the O-$K_\alpha$ fluorescence signal.[41] The computational domain is restricted to the pitch size of 100 nm. Periodic boundary conditions were assumed on the left and right sides of the nanostructure, while no geometrical variations were expected along the grating lines. During the reconstruction, these model parameters were changed and optimized within the domain boundaries listed in **Table 1**.

- **E-field calculation**: The calculation of the electric near-field was achieved by a finite-element method (FEM) Maxwell calculation. The whole computational domain was divided into a triangular mesh and the calculation was performed at the intersection points of the mesh.[42] The numerical accuracy of the simulated electric field is influenced by the choice of the discretization size d of the finite-elements and the degree p for the polynomial fit.[16] A discretization length of $d = 5$ nm and polynomial degree of $p = 4$ was chosen for the finite-element simulations, which is sufficient to ensure a minimal numerical error for the FEM simulations of the resulting electric field which is caused by the interaction of the incident light with the $Si_3N_4/SiO_2$ nanograting.[16] Figure 4b illustrates an exemplary result from a FEM calculation with the model from 4a and an incident beam with $E = 680$ eV, $\theta = 2°$ and $\varphi = 0°$. Showcased is the electric near-field intensity, which displays the distibution of the nodes and anti-nodes of the XSW field around the nanostructure. These nodes are confined in the grating groove, while also penetrating the near-surface area of the nanostructure. Changing the incident angle $\theta_i$ or azimuthal angle $\varphi$ will either move or change the shape of these nodes, allowing for a nm-sensitive probing of the nanostructure.
- **Fluorescence calculation**: The detected fluorescence photons emitted from the nanostructure can be theoretically calculated from the Sherman equation which is shown in Equation (3). Displayed is a modified version for 2D systems which contains all the experimentally determined quantities on the left side and all the theoretical/simulated quantities on the right side of the equation.[16]

$$\overbrace{\frac{4\pi \sin(\theta_i)}{\Omega(\theta_i)} \cdot \frac{\Phi(\theta_i, \varphi, E_i)}{\Phi_0 \epsilon_{\text{det}}(E_k)}}^{I_{\text{exp}}} = \overbrace{\frac{W_k \rho \tau(E_i) \omega_k}{\sum \mathrm{d}x} \cdot \sum_x \sum_y |E(x,y)|^2 \times e^{-\rho\mu(E_k)\gamma_{\text{dis}}(x,y)} \, \mathrm{d}x \, \mathrm{d}y}^{I_{\text{sim}}} \quad (3)$$

Fluorescence photons which are excited by the beam with incident angle $\theta_i$ can be detected under a solid angle $\Omega(\theta_i)/4\pi$. The measured fluorescence photon flux $\Phi(\theta_i, \varphi, E_i)$ depends on the incident beam energy $E_i$ and is further normalized by the incident photon flux $\Phi_0$ and the detector efficiency $\epsilon_{\text{det}}(E_k)$ at the fluorescence photon energy $E_k$. The left side of Equation (3) must now be simulated by performing a density integration over the fluorescent material. The prefactor incorporates the weight fraction $W_k$ and density $\rho$ of the material and the fundamental parameters such as the fluorescence yield $\omega_k$ and

**Table 1.** Interval boundaries for each model parameters which were used for the training data generation and for the reconstruction of the nanostructure.

| Model parameter | Domain boundaries |
|---|---|
| *h* / nm | [80, 115] |
| *cd* / nm | [28, 62] |
| *swa* / ° | [75, 90] |
| $t_{oxide}$ / nm | [1, 10] |
| $t_{groove}$ / nm | [1, 15] |

the energy dependent photoionization cross-section $\tau(E_i)$. The prior calculated electric near-field intensity distribution $|E(x, y)|^2$ is summed over the fluorescent material with taking an additional absorption term into consideration. The exponential damping factor incorporates the material density $\rho$, the mass attenuation coefficient $\mu(E_k)$ (dependent on the fluorescence line energy $E_k$) and the traveled path length $\gamma_{dis}(x, y)$ through the material.

- **Evaluate $\chi^2$ and optimization**: The $\chi^2$ is evaluated at each iteration step of the reconstruction process.

$$\chi^2(\vec{p}, \theta, \varphi) = \sum_{\theta,\varphi} \frac{\left(I_{sim}(\vec{p}, \theta, \varphi) - I_{exp}(\theta, \varphi)\right)^2}{\sigma_{exp}(\theta, \varphi)^2} \tag{4}$$

The simulated quantities $I_{sim}$ (right side of Equation 3) are compared against the experimental determined quantities $I_{exp}$ (left side of Equation 3) for a given model parameter set $\vec{p}$, incident angle $\theta$ and azimutal angle $\varphi$. $I_{sim}$ and $I_{exp}$ are further normalized accordingly to Equation (1), to make the reconstruction independent from uncertainties of the prefactors in Equation (3). The experimental error $\sigma_{exp}$ is incorporated into the weighting factor. To minimize $\chi^2$, an optimization algorithm is applied to search for the optimal model parameter vector $\vec{p}$. After each iteration step (in Figure 3), the reconstruction process starts from anew at the model assumption step (with a new model parameter vector $\vec{p}$). This loop is performed until a minimum is found for $\chi^2$ or a stopping criteria is met. The model parameter set $\vec{p}$, that minimizes Equation (4), is able to accurately describe the measured sample and thus represents the reconstructed nanostructure.

This reconstruction process is computational expensive and is massively impeded by the FEM calculation at the E-field calculation step. To circumvent the time consuming FEM calculation, a neural network model is utilized to directly predict the theoretical fluorescence intensities from an arbitrary model parameter set $\vec{p}$. This accelerates the whole reconstruction process and makes a reconstruction for multiple samples feasible.

### 3.2. Optimization Methods

An optimization algorithm was implemented to find the most probable solution among a wide set of possible choices, with the goal of minimizing Equation (4) during the reconstruction process. Among the diverse variety of techniques, Bayesian optimization (BO) and Markov Chain Monte Carlo (MCMC) stand out as powerful tools, each offering unique advantages.

The BO is an optimization technique that uses the principles of Bayesian inference to efficiently explore the parameter space.[43] Unlike traditional optimization methods, which often require a large number of evaluations to find the optimal solution, Bayesian optimization employs a probabilistic model to guide the search process.[44] The posterior probability $P(\vec{p}|I_{exp})$, of obtaining the geometrical parameter vector $\vec{p}$ within an observation of the experimental data $I_{exp}$, is given by

$$P(\vec{p}|I_{exp}) = \frac{P(I_{exp}|\vec{p})\, P(\vec{p})}{P(I_{exp})} \tag{5}$$

The probability $P(\vec{p})$ is attributed to prior knowledge from the geometrical parameters of $\vec{p}$. The model evidence $P(I_{exp})$ is difficult to compute, however, remains constant and does not affect the shape of the posterior distribution.[45] Bayesian optimization focuses on exploration on the most promising regions of the parameter space, which reduces the number of evaluations needed to find the most probable solution. This makes it well-suited for cases in which the evaluation of the likelihood function $P(I_{exp}|\vec{p})$ is very time-consuming. For that reason, the Bayesian optimization was employed during the reconstruction process which had a FEM forward calculation involved.

The MCMC allows for a general approach with a full exploration of the given parameter space.[46] Due to the computation speed of a NN calculation, the generality of the MCMC approach can be taken advantage of, which would have otherwise ended in a huge computational effort with the conventional FEM approach. The MCMC method constructs a Markov chain that explores the target distribution through an iterative sampling from a complex probability distribution.[46] By simulating a random walk through the parameter space, the MCMC is able to generate probability distributions that approximate the target distribution.[47] This makes it a more general method without any assumption of the posterior distribution. The optimization was performed by maximizing the logarithmic likelihood function

$$\ln(L) = -\frac{1}{2} \sum_i \left(\chi^2 + \ln(2\pi\sigma_{exp})\right) \tag{6}$$

## 4. Neural Network

### 4.1. Network Architecture and Training

A dataset of 14 000 nitrogen N-$K_\alpha$ and oxygen O-$K_\alpha$ fluorescence curves was generated for the neural network training. To ensure consistency with the experimental data, the generated curves were sampled across the same angular range. The required FEM calculations were performed using the parameterized nanostructure model introduced in Section 3.1. The geometrical parameter vector $\vec{p}$ served as input for the model and was uniformly sampled from the domains specified in Table 1. The resulting fluorescence intensities were also normalized by the mean value according to Equation (1).

The theoretical fluorescence intensities, needed for the nanostructure reconstruction, were predicted by an ensemble of two fully connected feed-forward neural networks. **Figure 5** showcases a schematic of the applied neural network architecture. Both networks have an input layer of 5 neurons (one for each of the geometrical model parameters), two hidden layers with 128 neurons (all layers with Rectified Linear Unit (ReLU) activation) and an output layer consisting of 162 neurons (with linear activation). Each output neuron describes the fluorescence intensities of either nitrogen N-$K_\alpha(\theta_i)$ or oxygen O-$K_\alpha(\theta_i)$ in dependence of

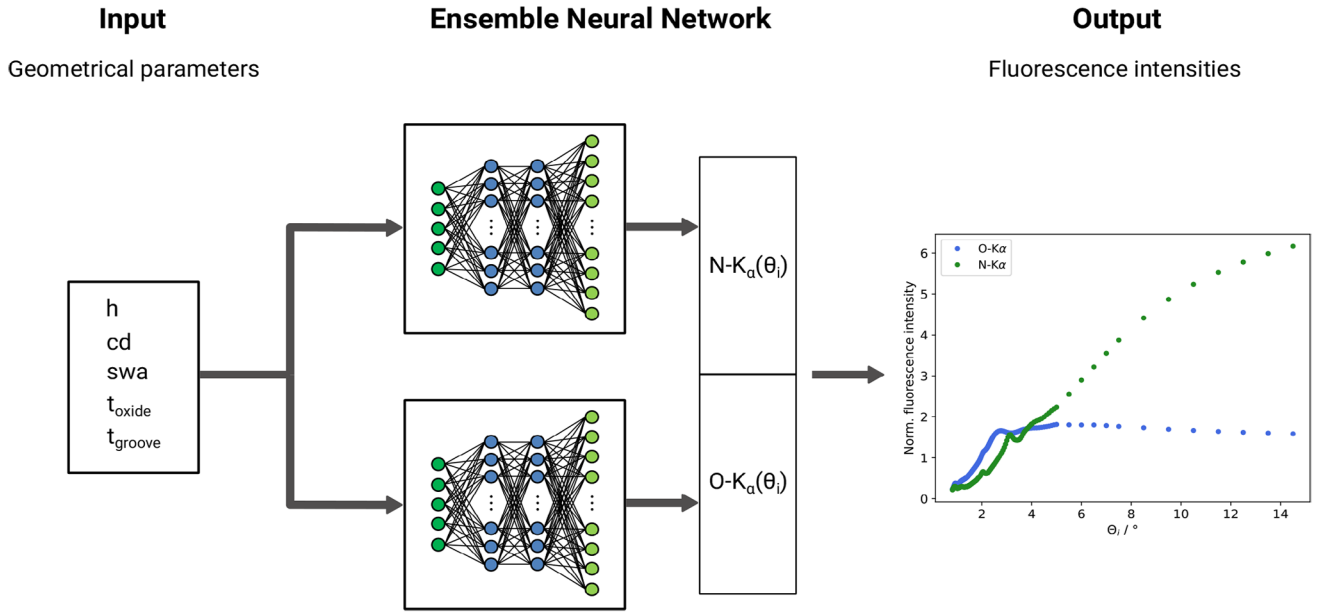


**Figure 5.** Schematic of the neural network architecture consisting of an ensemble of two fully-connected feed-forward neural networks. Each network receives the model parameters *h* (height), *cd* (width), *swa* (sidewall angle), thickness of $SiO_2$ layer on top $t_{oxide}$ and in the groove $t_{groove}$ as input parameters. The hidden layer consists of two fully-connected layers with each 128 neurons. The N-K$_\alpha$($\theta_i$) and O-K$_\alpha$($\theta_i$) fluorescence intensities for prior-defined $\theta_i$ angles are outputted from the network.

the incident angle $\theta_i$. The angular range between 0.82° and 5° is finely sampled with varying step sizes between 0.01° to 0.1° for the first 149 output neurons and the remaining 13 output neurons are attributed to the incident angles between 5° and 14.5° with step sizes of 0.5°, while the azimuthal angle was kept constant at $\varphi = 0°$. To ensure that both networks are not independently learning from each other, the outputs are eventually concatenated into one vector.[48,49]

The generated dataset was divided into a training, test and validation dataset within a 8:1:1 ratio. Training was performed with a batch size of 64, with batch normalization layers, a learning rate of $3 \cdot 10^{-4}$ and using the Adam optimizer.[50] The network predictions were compared to the ground truth fluorescence intensities derived from the FEM calculations under a mean squared error (MSE) loss function. The model had reached convergence after 900 epochs with a total training time of 20 min. The training routine and neural network model was implemented in PyTorch and performed on a NVIDIA TESLA P100 GPU.

### 4.2. Evaluation of Network Predictions

After successful training, the ensemble network is able to predict the N-K$_\alpha$($\theta_i$) and O-K$_\alpha$($\theta_i$) fluorescence intensities from a certain set of geometrical model parameters. **Figure 6a** showcases a comparison between the neural network prediction with the respective ground truth fluorescence intensities from the validation dataset.

The network is able to accurately predict the angular positions of the features and the further course of both the N-K$_\alpha$ and O-K$_\alpha$ fluorescence curves. An illustration of the relative deviations between the neural network prediction with the FEM

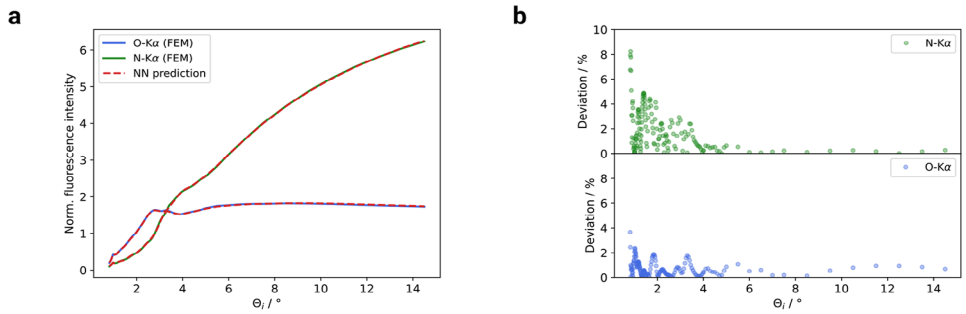


**Figure 6.** The ensemble neural network was trained to predict the N-K$_\alpha$($\theta_i$) and O-K$_\alpha$($\theta_i$) fluorescence intensities for a given geometrical parameter set. a) Comparison between the N-K$_\alpha$($\theta_i$) and O-K$_\alpha$($\theta_i$) fluorescence curves from the FEM calculation (blue and green) and the respective neural network prediction (red). b) Deviation (in %) between FEM calculation and NN prediction over the angular range.

**Table 2.** Average computation time for a calculation of the fluorescence curves.

| Computation time | |
|---|---|
| FEM calculation | NN calculation |
| 50 s | 3 ms |

calculation (for both N-$K_\alpha$ and O-$K_\alpha$) is shown in Figure 6b. In general, higher relative deviations can be observed for smaller angles below 4°, whereas for higher incident angles they tend to remain low. They can go up to 8% for N-$K_\alpha$ and up to 4% for O-$K_\alpha$. However, this study shows that for most incident angles, the neural network is able to accurately predict the fluorescence intensities with relative deviations below 2%. Overall, this is expected to have only a small influence on the reconstruction results, as these small fluorescence intensity deviations become negligible in comparison to the experimental errors shown in Figure 2.

## 5. Results and Discussion

### 5.1. Evaluation of Computation Time

An investigation on the feasibility of the NN implementation was conducted and evaluated in terms of computation speed. The FEM calculations were performed on multiple Intel(R) Xeon(R) Gold 6148 (2.40GHz) CPUs and Intel(R) Core(TM) i5-10400 (2.90GHz) CPUs, whereas calculations from the NN were performed on an Intel(R) Xeon(R) (2.20GHz) CPU with a NVIDIA Tesla P100 GPU. At first, the required computation time for a calculation of a fluorescence curve (over the whole angular range between 0.01° to 14.5°) was evaluated. **Table 2** displays the computation time needed to perform the forward calculations for each of the FEM and NN approaches.

Showcased is the average computation time, evaluated over multiple iterations of the forward calculation. It becomes evident that the NN achieved a significant reduction of the computation time, which is multiple orders of magnitude ($10^4$) faster compared to the conventional FEM calculation. This huge time gain massively reduces the overall computation time and can be exploited in the following reconstructions of the $Si_3N_4/SiO_2$ nanogratings.

**Figure 7** displays the $\chi^2$ values (Equation 4) over multiple iterations of the reconstruction process on one of the $Si_3N_4/SiO_2$ nanogratings. Also highlighted is the time required to reachconvergence during the reconstruction process for both the FEM and NN approach. It can be observed that the FEM approach requires more time for convergence in contrast to the NN approach. A time frame of at least 160 min was needed for the FEM approach to reach its minimum value $\chi^2_{minFEM}$, whereas the NN approach only took 23 s to converge to its minimum value $\chi^2_{minNN}$. A reduction of computation time was achieved by a factor of $10^2$ with utilizing the NN approach.

The results indicate that the NN reconstruction converges to a minimum that is close to the FEM approach solution. While the minimum $\chi^2$ value achieved by the FEM approach is slightly lower than that obtained by the NN, due to the intrinsic uncertainty of the NN, seen in Figure 6. This difference is expected to have a negligible impact on the final reconstructed model parameters, which is further confirmed by the reconstruction results from Section 5.3.

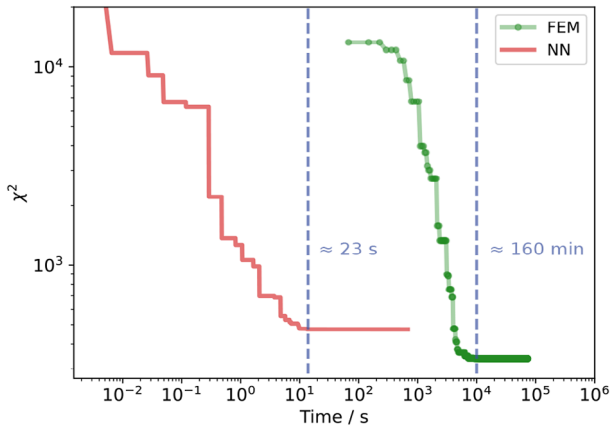


**Figure 7.** Time convergence study on the $Si_3N_4/SiO_2$ nanograting reconstructions. Showcased is the $\chi^2$ over the reconstruction time for both the FEM and NN approaches and their required time for convergence.

### 5.2. Confidence Intervals Evaluation

In order to estimate the reconstruction precision, the confidence intervals for the reconstructed model parameters were determined for both approaches. The FEM-based reconstruction utilizes a Bayesian optimization, where the confidence intervals are derived from the Hessian matrix with the model parameter set $\vec{p}$ that minimizes $\chi^2$

$$H_{ij} = \frac{\partial^2 \chi^2(\vec{p})}{\partial p_i \partial p_j} \tag{7}$$

The error covariance of the parameters is determined from the inverted Hessian matrix

$$C = H^{-1} \tag{8}$$

The confidence intervals can then be determined by[51]

$$\sigma_{\vec{p}} = \sqrt{\frac{\chi^2}{DOF}} \cdot \sqrt{\mathrm{diag}(H^{-1})} \tag{9}$$

with taking the degrees of freedom DOF = $N - M$ (N number of inputs/measurement points, M number of free parameters) into account.

For the NN-based reconstruction, confidence intervals were estimated from an empiric study using simulated data from the test dataset. Multiple reconstructions were performed on the simulated fluorescence curves (with simulated errors) from the test dataset, where the corresponding geometrical parameter vector served as the target. Deviations between the targeted geometrical parameters and the reconstructed model parameters were averaged over the number of reconstructions. This gives an estimation on the percentage error for each model parameter for the

**Table 3.** Average confidence intervals for the reconstructed model parameters when utilizing the NN approach.

| | *h* | *cd* | *swa* | $t_{oxide}$ | $t_{groove}$ |
|---|---|---|---|---|---|
| Confidence intervals | 1.8% | 1% | 0.6% | 3.9% | 5.0% |

NN-based reconstruction, summarized in **Table 3**. It becomes apparent that the utilized method has a different sensitivity for certain model parameters. A higher uncertainty is expected in the reconstruction of the height $h$ of the $Si_3N_4$ nanostructure and the oxide thicknesses $t_{oxide}$ and $t_{groove}$ of the $SiO_2$ layer.

Due to the sheer size of the $Si_3N_4$ structure, modes of the XSW are not able to fully probe the whole material. Especially material positioned at the bottom center of the nanostructure will be less excited by the XSW field due to absorption effects. The nitrogen fluorescence signal coming from this region contains additional information about the height of the nanostructure, which is eventually missing for the exact determination of this quantity.

Also the exact determination of the oxide thicknesses is impeded by the limitation of the GIXRF approach which is particular at grazing angles. The reconstructed oxide thicknesses are mainly derived from the oxygen fluorescence signal at grazing angles, where a high sensitivity prevails for the surface. Particularly at these angles, the solid angle error $\sigma_\Omega$ dominates the total experimental error $\sigma_{exp}$ due to the over-illumination of the sample and the strong influence of small sample alignment errors. This effect was also considered in the simulated fluorescence curves from the test dataset. Consequently, this heavily impedes a correct determination of the oxide layer thicknesses, contributing to the observed discrepancy. It was also shown before in Section 4.2 that the NN displayed an inability to accurately predict the fluorescence intensity for very small angles. This is crucial for the determination of a thin oxide layer thickness, which also leads to a mismatch of the obtained oxide thicknesses.

### 5.3. Reconstruction Results

The reconstructions were performed on the three distinct $Si_3N_4/SiO_2$ nanogratings, whereas the highest variation is anticipated in the width (*cd*) parameter. Optimizations were performed by continuously comparing the experimental data against forward calculated fluorescence curves derived from the FEM and NN computations. These optimizations were conducted until Equation (4) converged to a minimum, denoting the geometric parameters of the nanostructure that most accurately describe the experimental data.

**Table 4** summarizes the obtained geometrical parameters of all investigated nanostructures and showcases a direct comparison between the FEM and NN reconstruction approach. It becomes evident that across all three nanogratings, the NN approach was able to determine the geometrical parameters close to the FEM-based optimization, while only needing a small fraction of computation time. All the reconstructed parameters are overlapping within their respective 1-$\sigma$ confidence intervals with their FEM-based counterparts. A maximum deviation of up to 4.3% can be observed for $t_{oxide}$ of sample 1, whereas the other relative deviations remain below that. These results demonstrate that the NN is a suitable substitution for the time-consuming FEM calculation. A drastically reduced computation time was required for the reconstructions, with higher confidence intervals as consequence in comparison to the FEM approach.

The anticipated model parameter sensitivity, discussed in Section 5.2, was also demonstrated by the reconstruction results. However the height $h$ of the $Si_3N_4$ nanostructure, the oxide thicknesses $t_{oxide}$ and $t_{groove}$ generally display a higher discrepancy between the reconstruction approaches. It is also noteworthy to emphasize that the utilized nanostructure model assumed a discrete oxide layer with a sharp transition to the layers underneath. Incorporating an interdiffusion layer can enhance the accuracy of the model system. The inclusion of such a layer, characterized by a compositional gradient of the respective elements across the interfaces, has already demonstrated promising results in the reconstruction of layered structures.[52,53] However, simulations of layered systems are computationally less demanding, as they can be efficiently handled using methods such as the Transfer-Matrix Method. In contrast, for more complex nanostructures, such as nanogratings, the introduction of interdiffusion layers introduces additional free parameters in the reconstruction process, significantly increasing the computational effort. To mitigate this, a simplified model assuming a sharp interface transition was employed, reducing the number of free parameters and ensuring computational feasibility.

Also for the third nanograting, a higher nominal $t_{groove}$ thickness is noticeable compared to the other nanogratings. This is due to the simplified nanostructure model that does not account for overetching effects into the silicon substrate. During the etching process (within the manufacturing step), an overetching into the silicon substrate might occur. The oxide layer along the sidewall would have been extended, leading into a contribution to the total oxygen fluorescence signal. This effect was not considered

**Table 4.** Reconstructed model parameters for the three different nanograting samples. Each nanograting was reconstructed by a FEM-based and a NN-based forward calculation. The 1-$\sigma$ confidence intervals are given for each respective model parameter value.

| | Nanograting 1 | | | Nanograting 2 | | | Nanograting 3 | | |
|---|---|---|---|---|---|---|---|---|---|
| Model parameter | FEM | NN | rel. deviation | FEM | NN | rel. deviation | FEM | NN | rel. deviation |
| *h* / nm | 98.0 (3) | 97 (2) | 1% | 96.3 (3) | 98 (2) | 1.8% | 97 (2) | 100 (2) | 3% |
| *cd* / nm | 49.85 (5) | 49.4 (5) | 0.9% | 47.2 (5) | 46.4 (4) | 1.7% | 62.6 (1) | 62.9 (6) | 0.1% |
| *swa* / ° | 83.6 (1) | 83.8 (4) | 0.02% | 82.7 (1) | 82.9 (4) | 0.4% | 84.0 (1) | 83.5 (4) | 0.1% |
| $t_{oxide}$ / nm | 2.58 (3) | 2.47 (8) | 4.3% | 2.17 (1) | 2.23 (8) | 2.4% | 2.72 (2) | 2.72 (9) | 0% |
| $t_{groove}$ / nm | 6.0 (1) | 5.9 (3) | 1.7% | 5.1 (2) | 5.0 (3) | 2% | 12.5 (1) | 12.3 (7) | 2% |

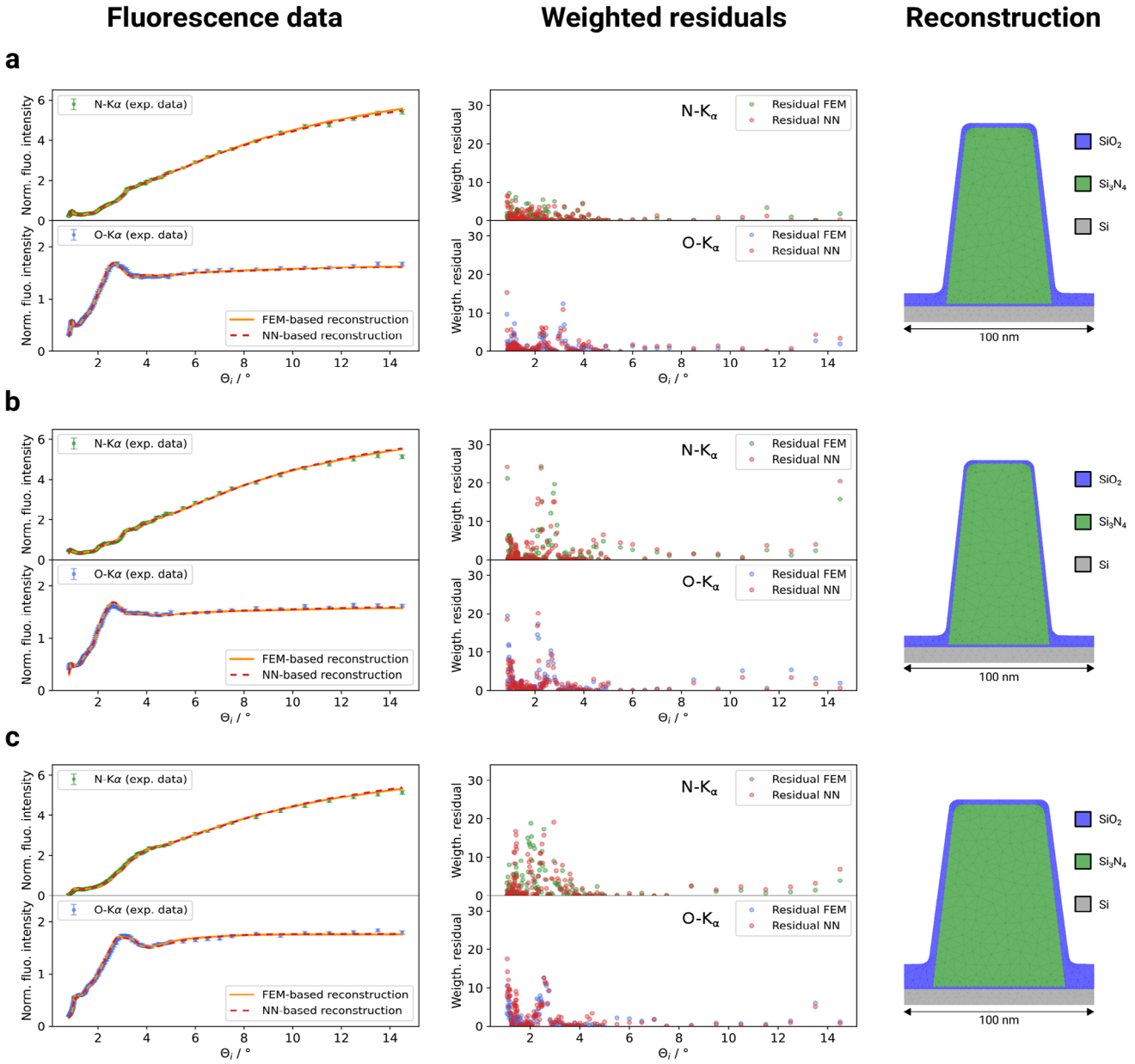


**Figure 8.** Reconstruction results of the three investigated nanogratings. a) Nanograting 1: (Left) Comparison of the exp. data with the forward-calculated fluorescence curves. The forward calculations were performed with the obtained geometrical parameters from the FEM (yellow line) and NN (red dashed-line) reconstruction approach. (Middle) Weighted residuals between the exp. N-K$_\alpha$($\theta_i$) and O-K$_\alpha$($\theta_i$) fluorescence intensities and the FEM- and NN-based values. (Right) Reconstructed model of the $Si_3N_4/SiO_2$ nanograting with the obtained parameter values from the NN reconstruction. Respectively for b) nanograting 2 and c) nanograting 3.

in the showcased nanostructure model, implying a compensation of the missing oxygen fluorescence signal by an increasement of the oxide layer thickness inside the groove (inbetween the grating lines). However this does not affect the performance of the NN approach, which was able to determine a groove oxide layer thickness close the the FEM approach.

**Figure 8** displays the reconstruction results of all three nanogratings and gives insights about the accuracy of the respective reconstruction approaches. The results for the first nanograting are summarized in Figure 8a, where the fluorescence fits, their respective weighted residuals and the reconstructed nanogratings are shown. Illustrated (on the left side) is a comparison between the experimental determined N-K$_\alpha$($\theta_i$) and O-K$_\alpha$($\theta_i$) fluorescence intensities (normalized by the mean value) and the simulated fluorescence intensities of the nanograting model. The reconstructed geometrical parameters from Table 4 were utilized to perform the forward calculation (by FEM) for both reconstruction approaches.

Notably here is, that the simulated fluorescence curves from both reconstruction approaches precisely align with the

experimental data. Both the FEM-based reconstruction (orange curve) and NN-based reconstruction (red curve) have the same course of behavior, with only small deviations inbetween. This becomes more apparent with the consideration of their weighted residuals from the experimental data (figure in the center). The weighted residuals were calculated in respect to Equation (4) and were eventually displayed for each measured incident angle $\theta_i$. For small incident angles, the weighted residuals tend to be bigger in comparison to higher angles of incidence. On the one hand, this shows the limitation of the GIXRF method, where the over-illumination of the sample at grazing incident angles remain a challenge. On the other hand, are the absolute intensity values at grazing angles very small, which translate to a high error contribution from the counting statistic. Additionally, small angle offsets from the sample alignment can couple in, which have a significant effect on the course of the curves for grazing angles.

The reconstruction results for the second and third nanograting are summarized in Figure 8b,c and display a similar behaviour as the previous nanograting. The fluorescence intensities from the NN method approximate the experimental data accurately and align well with their FEM-based counterpart. The weighted residuals showcase the same behaviour for both approaches and imply an accurate emulation of the NN approach.

## 6. Conclusion

This work has shown a reduction of computation time by a factor of $10^4$ for the forward calculation and a factor of $10^2$ for the reconstruction of periodic nanostructures, by utilizing a NN model instead of the FEM calculation inside the reconstruction process. It was demonstrated that the NN model is a well-suited substitute for the time-consuming FEM calculations which were required in the previous reconstruction method. At first, the performance of the network was benchmarked on simulated data from FEM calculations and was subsequently examined on experimental data from GIXRF measurements. The accurate GIXRF based characterization of three $Si_3N_4/SiO_2$ nanogratings (with varying geometrical parameters) demonstrates the feasibility of the drastically faster NN approach. For all three nanogratings, a good agreement between the FEM and NN based reconstruction results was found, with all reconstructed geometrical parameters being consistent within their determined confidence intervals. The anticipated width variation of these nanostructures was well captured and showcased in the reconstruction results. This was all achieved by the NN within a small fraction of computation time which was otherwise required for FEM approach. The time saved could be further improved with the usage of GPUs, which have a higher scalability compared to calculations performed on CPUs.

However with the GIXRF setup, the measured signal is especially susceptible to the over-illumination of the sample. Measurements with GEXRF eliminate the over-illumination of the sample due to the near-normal angle of incidence of the excitation beam, making this technique favorable for future semiconductor metrology applications. The approach to substitute the time-consuming FEM calculation with the NN model can be easily transferred to this kind of measurement and enable a new route for fast reconstruction evaluations. The reduced computation time enables a possibility to reconstruct multiple similar nanostructures within a small time frame, which would be mandatory in an industrial environment. It is one necessary step to enable a more practical application of X-ray fluorescence based metrology for a non-destructive, element-specific and surface-sensitive characterization of nanostructured samples.

## 7. Experimental Section

*Fabrication of $Si_3N_4/SiO_2$ Nanogratings*: Subject of the investigation are three $Si_3N_4/SiO_2$ line gratings which were manufactured at Helmholtz–Zentrum Berlin (HZB). A silicon wafer with a 100 nm $Si_3N_4$ layer on top was used as base substrate for the manufacturing. The line patterning was achieved through electron beam lithography (EBL). For this, a positive resist (ZEP520A) was spin-coated on the substrate and subsequently exposed with a e-beam writer (Vistec EBPG5000+). The line gratings were obtained after reactive ion etching with $CHF_3$ and a following oxygen plasma cleaning step for photoresist residues. All gratings have the same pitch of $p = 100$ nm and approximately the same nominal height $h$. The three gratings were purposely manufactured with different nominal widths $cd$ around 40 – 45 nm, 50 nm and 60 nm. Due to the manufacturing process, slight variations on the height, widths and sidewall angle are possible. On each sample, the whole patterned area amounts to 1 mm × 15 mm, whereas the remaining area around consists of the initial $Si_3N_4$ layer.

*Determination of Optical Constants*: The optical constants of the $Si_3N_4$ and $SiO_2$ layers (incident energy of $E = 680$ eV) were previously determined with X-ray reflectometry (XRR) and are assumed for further simulations in this work.[24] For the $Si_3N_4$ layer, a $\delta = (12.59 \pm 0.05) \cdot 10^{-4}$ and $\beta = (2.58 \pm 0.02) \cdot 10^{-4}$ was acquired, whereas for the $SiO_2$ layer, the optical constant were determined to $\delta = (8.73 \pm 0.03) \cdot 10^{-4}$ and $\beta = (2.58 \pm 0.04) \cdot 10^{-4}$.

## Acknowledgements

The authors would like to thank Jürgen Probst for the manufacturing of the $Si_3N_4/SiO_2$ nanogratings. The project (grant agreement number 101096772) is supported by Chips Joint Undertaking and its members, including the top-up funding of Belgium and the Netherlands. Funded by the European Union.

## Conflict of Interest

The authors declare no conflict of interest.

## Data Availability Statement

The data that support the findings of this study are available from the corresponding author upon reasonable request.

## Keywords

finite element method, machine learning, nanostructure characterization, neural network, X-ray fluorescence

Received: November 11, 2024
Revised: March 20, 2025
Published online: April 29, 2025

[1] W. Cao, H. Bu, M. Vinet, M. Cao, S. Takagi, S. Hwang, T. Ghani, K. Banerjee, *Nature* **2023**, *620*, 501.

[2] S. Wang, X. Liu, P. Zhou, *Adv. Mater.* **2022**, *34*, 2106886.
[3] G. Moore, *Electronics Magazine* **1965**, *38*, 114.
[4] N. G. Orji, M. Badaroglu, B. M. Barnes, C. Beitia, B. D. Bunday, U. Celano, R. J. Kline, M. Neisser, Y. Obeng, A. Vladar, *Nat. Electron.* **2018**, *1*, 532.
[5] C. Shin, *Variation-aware advanced CMOS devices and SRAM*, vol. *56*, Springer, **2016**.
[6] N. Loubet, T. Hook, P. Montanini, C.-W. Yeung, S. Kanakasabapathy, M. Guillom, T. Yamashita, J. Zhang, X. Miao, J. Wang, et al., in *2017 symposium on VLSI technology*, IEEE, **2017**, pp. T230–T231.
[7] R. Ritzenthaler, H. Mertens, G. Eneman, E. Simoen, E. Bury, P. Eyben, F. Bufler, Y. Oniki, B. Briggs, B. Chan, et al., in *2021 IEEE International Electron Devices Meeting (IEDM)*, IEEE, **2021**, pp. 26–2.
[8] H. Mertens, M. Hosseini, T. Chiarella, D. Zhou, S. Wang, G. Mannaert, E. Dupuy, D. Radisic, Z. Tao, Y. Oniki, et al., in *2023 IEEE Symposium on VLSI Technology and Circuits (VLSI Technology and Circuits)*, IEEE, **2023**, pp. 1–2.
[9] T.-F. Yao, A. Duenner, M. Cullinan, *Precision Engineering* **2017**, *47*, 147.
[10] L. Kwakman, A. Kenslea, H. Johanesen, J. Cramer, M. Strauss, W. Boullart, H. Mertens, Y. K. Siew, K. Barla, in *Metrology, Inspection, and Process Control for Microlithography XXXIII*, vol. *10959*, SPIE, **2019**, pp. 47–60.
[11] K. Ueda, S. Koshihara, T. Mizuno, A. Miura, in *Metrology, Inspection, and Process Control for Microlithography XXV*, vol. *7971*, SPIE, **2011**, pp. 613–621.
[12] P. Linkov, M. Artemyev, A. E. Efimov, I. Nabiev, *Nanoscale* **2013**, *5*, 8781.
[13] T. Choisnet, A. Hammouti, V. Gagneur, J. Reche, G. Rademaker, G. Freychet, G. Jullien, J. Ducote, P. Gergaud, D. Le Cunff, in *Metrology, Inspection, and Process Control XXXVII*, vol. *12496*, SPIE, **2023**, pp. 428–437.
[14] V. Soltwisch, A. Fernández Herrero, M. Pflüger, A. Haase, J. Probst, C. Laubis, M. Krumrey, F. Scholze, *J. Appl. Crystallogr.* **2017**, *50*, 1524.
[15] A. F. Herrero, M. Pflüger, J. Puls, F. Scholze, V. Soltwisch, *Opt. Express* **2021**, *29*, 35580.
[16] V. Soltwisch, P. Hönicke, Y. Kayser, J. Eilbracht, J. Probst, F. Scholze, B. Beckhoff, *Nanoscale* **2018**, *10*, 6177.
[17] P. Hönicke, Y. Kayser, K. V. Nikolaev, V. Soltwisch, J. E. Scheerder, C. Fleischmann, T. Siefke, A. Andrle, G. Gwalt, F. Siewert, et al., *Small* **2022**, *18*, 2105776.
[18] Y. Kayser, P. Hönicke, D. Banaś, J.-C. Dousse, J. Hoszowska, P. Jagodziński, A. Kubala-Kukuś, S. H. Nowak, M. Pajek, *J. Anal. At. Spectrom.* **2015**, *30*, 1086.
[19] P. Hönicke, B. Beckhoff, M. Kolbe, D. Giubertoni, J. van den Berg, G. Pepponi, *Anal. Bioanal. Chem.* **2010**, *396*, 2825.
[20] J. Baumann, Y. Kayser, B. Kanngießer, *Phys. Status Solidi B* **2021**, *258*, 2000471.
[21] B. Pollakowski, B. Beckhoff, F. Reinhardt, S. Braun, P. Gawlitza, *Physical Review B–Condensed Matter and Materials Physics* **2008**, *77*, 235408.
[22] J. Zegenhagen, A. Kazimirov, *X-ray Standing Wave Technique, The: Principles And Applications*, vol. *7*, World Scientific, **2013**.
[23] K. Matveevskii, K. V. Nikolaev, R. Fallica, D. Beckers, M. Gateshki, A. Kharchenko, B. Spanjer, A. Rogachev, S. Yakunin, M. Ackermann, et al., *Appl. Crystallogr.* **2024**, *57*, 5.
[24] A. Andrle, P. Hönicke, G. Gwalt, P.-I. Schneider, Y. Kayser, F. Siewert, V. Soltwisch, *Nanomaterials* **2021**, *11*, 1647.
[25] P. Hönicke, A. Andrle, Y. Kayser, K. V. Nikolaev, J. Probst, F. Scholze, V. Soltwisch, T. Weimann, B. Beckhoff, *Nanotechnology* **2020**, *31*, 505709.
[26] S. Staeck, A. Andrle, P. Hönicke, J. Baumann, D. Grötzsch, J. Weser, G. Goetzke, A. Jonas, Y. Kayser, F. Förste, et al., *Nanomaterials* **2022**, *12*, 3766.
[27] J. Pomplun, S. Burger, L. Zschiedrich, F. Schmidt, *Phys. Status Solidi B* **2007**, *244*, 3419.
[28] L. G. Wright, T. Onodera, M. M. Stein, T. Wang, D. T. Schachter, Z. Hu, P. L. McMahon, *Nature* **2022**, *601*, 549.
[29] M. Maurizi, C. Gao, F. Berto, *Sci. Rep.* **2022**, *12*, 21834.
[30] Y. LeCun, Y. Bengio, G. Hinton, *Nature* **2015**, *521*, 436.
[31] S. Yu, J.-S. Yu, Z. Chen, Q. Li, Z. Wang, X. Luo, S.-K. Kim, R. Hu, *ACS Photonics* **2024**, *11*, 3412.
[32] S. Yu, P. Zhou, W. Xi, Z. Chen, Y. Deng, X. Luo, W. Li, J. Shiomi, R. Hu, *Light: Sci. Appl.* **2023**, *12*, 291.
[33] J. Lim, D. Psaltis, *Apl Photonics* **2022**, *7*, 1.
[34] Y. Chen, L. Lu, G. E. Karniadakis, L. Dal Negro, *Opt. Express* **2020**, *28*, 11618.
[35] J. Jiang, M. Chen, J. A. Fan, *Nat. Rev. Mater.* **2021**, *6*, 679.
[36] R. Becker, J. A. Golovchenko, J. Patel, *Phys. Rev. Lett.* **1983**, *50*, 153.
[37] R. Klockenkämper, A. Von Bohlen, *Total-reflection X-ray fluorescence analysis and related methods*, John Wiley & Sons, **2014**.
[38] B. Beckhoff, A. Gottwald, R. Klein, M. Krumrey, R. Müller, M. Richter, F. Scholze, R. Thornagel, G. Ulm, *Phys. Status Solidi B* **2009**, *246*, 1415.
[39] F. Senf, U. Flechsig, F. Eggenstein, W. Gudat, R. Klein, H. Rabus, G. Ulm, *J. Synchrotron Radiat.* **1998**, *5*, 780.
[40] J. Lubeck, B. Beckhoff, R. Fliegauf, I. Holfelder, P. Hönicke, M. Müller, B. Pollakowski, F. Reinhardt, J. Weser, *Rev. Sci. Instrum.* **2013**, *84*, 4.
[41] A. Andrle, *Doctoral dissertation*, Technische Universität Berlin, **2023**.
[42] P. Monk, *Finite element methods for Maxwell's equations*, Oxford university press, **2003**.
[43] P. I. Frazier, in *Recent advances in optimization and modeling of contemporary problems*, Informs, **2018**, pp. 255–278.
[44] M. Pelikan, M. Pelikan, IEEE **2005**, pp. 31–48.
[45] P.-I. Schneider, X. Garcia Santiago, V. Soltwisch, M. Hammerschmidt, S. Burger, C. Rockstuhl, *ACS Photonics* **2019**, *6*, 2726.
[46] R. M. Neal, *Probabilistic inference using Markov chain Monte Carlo methods*, Department of Computer Science, University of Toronto, **1993**.
[47] S. Brooks, *J. Royal Stat. Soc.: Series D (the Statistician)* **1998**, *47*, 69.
[48] K. M. R. Alam, N. Siddique, H. Adeli, *Neural Comput. Appl.* **2020**, *32*, 8675.
[49] L. K. Hansen, P. Salamon, *IEEE Trans. Pattern Analysis Mach. Intell.* **1990**, *12*, 993.
[50] D. P. Kingma, *arXiv preprint arXiv:1412.6980* **2014**.
[51] C. E. Rasmussen, *Gaussian processes in machine learning*, Springer, **2003**.
[52] R. Ciesielski, J. Bogdanowicz, R. Loo, Y. Shimura, A. Mani, C. Mitterbauer, M. Kolbe, V. Soltwisch, *J. Micro/Nanopatterning, Materials, Metrology* **2024**, *23*, 041405.
[53] P. Hönicke, B. Detlefs, E. Nolot, Y. Kayser, U. Mühle, B. Pollakowski, B. Beckhoff, *J. Vac. Sci. Technol., A* **2019**, *37*, 4.